

An emission-state-switching radio transient with a 54-minute period

Received: 1 February 2024

Accepted: 25 April 2024

Published online: 05 June 2024

 Check for updates

M. Caleb^{1,2,17}✉, E. Lenc^{3,17}✉, D. L. Kaplan⁴, T. Murphy^{1,2}, Y. P. Men⁵, R. M. Shannon⁶, L. Ferrario⁷, K. M. Rajwade^{8,9}, T. E. Clarke¹⁰, S. Giacintucci¹⁰, N. Hurley-Walker¹¹, S. D. Hyman¹², M. E. Lower³, Sam McSweeney¹¹, V. Ravi^{13,14}, E. D. Barr⁵, S. Buchner¹⁵, C. M. L. Flynn⁶, J. W. T. Hessels⁸, M. Kramer⁶, J. Pritchard¹ & B. W. Stappers¹⁶

Long-period radio transients are an emerging class of extreme astrophysical events of which only three are known. These objects emit highly polarized, coherent pulses of typically a few tens of seconds duration, and minutes to approximately hour-long periods. Although magnetic white dwarfs and magnetars, either isolated or in binary systems, have been invoked to explain these objects, a consensus has not emerged. Here we report on the discovery of ASKAP J193505.1+214841.0 (henceforth ASKAP J1935+2148) with a period of 53.8 minutes showing 3 distinct emission states—a bright pulse state with highly linearly polarized pulses with widths of 10–50 seconds; a weak pulse state that is about 26 times fainter than the bright state with highly circularly polarized pulses of widths of approximately 370 milliseconds; and a quiescent or quenched state with no pulses. The first two states have been observed to progressively evolve over the course of 8 months with the quenched state interspersed between them suggesting physical changes in the region producing the emission. A constraint on the radius of the source for the observed period rules out an isolated magnetic white-dwarf origin. Unlike other long-period sources, ASKAP 1935+2148 shows marked variations in emission modes reminiscent of neutron stars. However, its radio properties challenge our current understanding of neutron-star emission and evolution.

ASKAP J1935+2148 was serendipitously discovered during a target of opportunity observation of the gamma-ray burst GRB 221009A with the Australian Square Kilometre Array Pathfinder (ASKAP) telescope. Bright pulses of radio emission from ASKAP J1935+2148 were seen on 15 October 2022 using a fast-imaging technique on images with 10 s integration times (Methods). ASKAP J1935+2148 is located at right ascension (J2000) 19 h 35 min 05.126 s \pm 1.5" and declination (J2000) +21° 48' 41.047" \pm 1.5", which is coincidentally 5.6' from the magnetar SGR 1935+2154 and sits on the edge of the supernova remnant in which SGR 1935+2154 is centred. The observation lasted ~6 h, revealing 4 bright pulses lasting 10–50 s in the images, with the brightest peak

pulse flux density measuring 119 mJy. Inspection of the light curves of the pulses revealed a tentative period of ~54 min.

In addition to a weak detection in an archival ASKAP observation, the source was consistently detected in four follow-up observations. A summary of all observations with ASKAP is presented in Extended Data Table 1. Overall, the pulses are visible across the whole bandpass-corrected observing band of 288 MHz, leading to a spectral index estimation of $\alpha \approx +0.4 \pm 0.3$ at 887.5 MHz. However, a dispersion measure (DM) constraint/estimate was not possible due to the coarse time resolution of 10 s. We quantify the pulses to be >90% linearly polarized—implying strongly ordered magnetic fields, with a rotation

measure (RM) of $+159.3 \pm 0.3 \text{ rad m}^{-2}$ calculated using the RM synthesis method¹. In comparison, the RM and DM of SGR 1935+2154 are approximately $+107 \text{ rad m}^{-2}$ and approximately 330 pc cm^{-3} , respectively². The RM of ASKAP J1935+2148 is consistent with the contribution from the smoothed Galactic foreground³ and with those of nearby pulsars (<https://www.atnf.csiro.au/research/pulsar/psrcat/>), precluding the presence of a substantial RM imparted at the source.

Following the discovery, we conducted simultaneous beamformed and imaging follow-up observations at 1,284 MHz with the MeerKAT radio interferometer (Methods). Two pulses were detected in both the beamformed and imaging data in two independent observations (Extended Data Table 1). The initial estimate of period allowed us to predict the times of arrival (ToAs) of future pulses at the same rotational phase of ASKAP J1935+2148, and the MeerKAT pulses are observed to arrive within 319 ms of the predicted times (that is, within 10^{-4} of a period). The ToAs of all the ASKAP and MeerKAT detections were used to determine a phase-connected timing solution with a period P of $3,225.313 \pm 0.002 \text{ s}$ (Methods and Fig. 1), and an upper limit on the period derivative, \dot{P} of $\leq (1.2 \pm 1.5) \times 10^{-10} \text{ s s}^{-1}$ with a 1σ error. The location of ASKAP J1935+2148 in the $P - \dot{P}$ parameter space, which is frequently used to classify different sorts of pulsars, is consistent with other known long-period sources (Extended Data Fig. 1). ASKAP J1935+2148 is seen to reside in the pulsar death valley where detectable radio signals are not expected, challenging currently accepted theories of radio emission via spin-down (Extended Data Fig. 1). The radio properties of ASKAP J1935+2148 are presented in Table 1.

A first single pulse was detected by the MeerTRAP real-time detection system (Methods) on 3 February 2023 with a DM of $145.8 \pm 3.5 \text{ pc cm}^{-3}$ and a width of $\sim 370 \text{ ms}$ (Extended Data Table 1), which is ~ 135 times narrower than the brightest ASKAP pulse. Contrary to the ASKAP duty cycle of 1.5%, the narrow width of the MeerKAT pulse results in a duty cycle of only 0.01%. The average DM inferred distance based on the NE2001⁴ and YMW16⁵ Galactic electron density models places ASKAP J1935+2148 at a distance of 4.85 kpc (Table 1). The detection is accompanied by weak pre- and post-cursor pulses, as seen in Fig. 2. The data recorded to disk with the PTUSE backend (Methods) did not reveal a broader underlying emission envelope similar to the wide pulse widths seen in the ASKAP detections. The corresponding MeerKAT 2-s-resolution image (the shortest possible timescale) revealed a single 9 mJy detection, which is ~ 26 times fainter than the brightest ASKAP pulse. The pulse was localized to right ascension (J2000) $19 \text{ h } 35 \text{ min } 05.175 \text{ s} \pm 0.3''$ and declination (J2000) $+21^\circ 48' 41.504'' \pm 0.6''$, which is consistent with the ASKAP coordinates. Throughout the paper, the flux densities quoted for the MeerKAT data are from the images as the beamformed data are only polarization and not flux calibrated. Unlike the ASKAP pulses, our MeerKAT detection revealed a substantial circular polarization fraction exceeding 70%, coupled with a linear polarization fraction of $\sim 40\%$. We did not find evidence for Faraday conversion (Methods). In addition to being spatially coincident, the measured RM of $+159.8 \pm 0.3 \text{ rad m}^{-2}$ agrees with that measured for the ASKAP detections, giving us added confidence that despite the drastically different pulse widths, the ASKAP and MeerKAT detections were produced by the same object.

The second MeerKAT detection was made on 8 May 2023 with a flux density of 2.9 mJy averaged over 2 s (Extended Data Table 1). This burst was also $\sim 370 \text{ ms}$ wide and highly circularly polarized with no broader emission envelope, but the lack of sufficient signal to noise precluded a reliable RM estimation. Both MeerKAT pulses are visible across the whole 856 MHz band with a spectral index estimate of $\alpha \approx -1.2 \pm 0.1$ at 1,284 MHz. Such variations in spectral indices have been observed in both pulsars and radio magnetars showing different emission states^{6,7}. Combining all the ASKAP and MeerKAT observations (Extended Data Table 1), we see that the source is not detectable in every

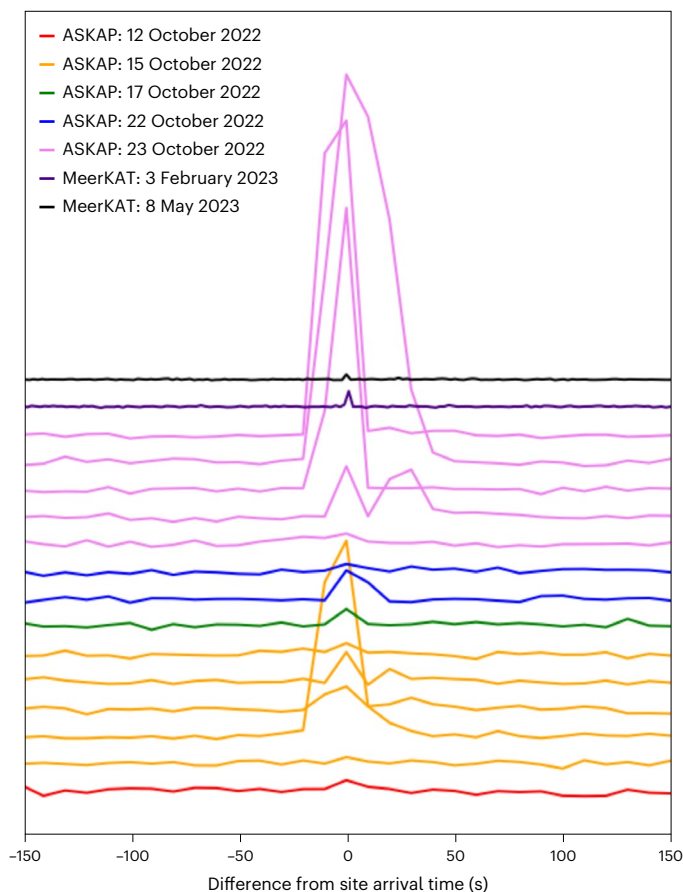


Fig. 1 | Light curves of the ASKAP and MeerKAT detections. The y-axis is the pulse number. The peak flux densities of these detections are reported in Extended Data Table 1. The different colours represent the dates of the observations. Pulse detections within an observation represent consecutive rotations of the source. Although different in terms of radio properties, the MeerKAT detections appear to arrive in phase with the ASKAP detections.

single observation indicating intermittency, potential nulling where the pulsed emission temporarily ceases or becomes undetectable, or drastic variations in flux density. Using epochs 1 to 17 in Extended Data Table 1, we estimate the source to be in a quenched or quiescent state ~ 40 – 50% of the time, at MeerKAT and ASKAP.

Observationally, ASKAP J1935+2148 appears to show three emission states:

- (1) The strong pulse mode consisting of 15 bright, tens-of-seconds-wide and highly linearly polarized pulses as seen with ASKAP
- (2) The weak pulse mode characterized by two faint, hundreds-of-milliseconds-wide and highly circularly polarized pulses as seen with MeerKAT
- (3) The completely nulling or quiescent mode as seen with both telescopes

We consider two possible scenarios for the observed differences in properties of the ASKAP and MeerKAT bursts.

In the first scenario, the ASKAP pulses could span only a small fraction (that is a few hundreds of milliseconds) of the shortest possible time resolution of 10 s. This scenario would imply that the source produces only subsecond-duration pulses. In Fig. 1, we see the flux densities of detections from 10 s ASKAP images to gradually rise and fall, resulting in an almost Gaussian-like pulse profile. This distribution of the flux densities makes it unlikely for the burst to be composed of several consecutive millisecond-duration pulses. However, it remains possible for subsecond-timescale structure to be superimposed on the broader emission envelope.

Table 1 | Measured and derived radio quantities for ASKAP J1935+2148 from the ASKAP and MeerKAT observing campaigns

Parameter	ASKAP	MeerKAT
Centre frequency	887.5 MHz	1,284 MHz
Bandwidth	288 MHz	856 MHz
Imaging time resolution	10 s	2 s
Beamformed time resolution	–	38.28 μ s
Typical widths, W	10–50 s	~370 ms
Linear polarization fraction, L/I	>90%	~40%
Circular polarization fraction, V/I	<3%	>70%
Inband spectral index, α	+0.4 \pm 0.3	–1.2 \pm 0.1
Rotation measure, RM	+159.3 \pm 0.3 rad m ^{–2}	+159.1 \pm 0.3 rad m ^{–2}
Peak flux density of brightest pulse, S_{ν}	234.7 mJy	9 mJy
Radio luminosity, L_{ν}	1.8 \times 10 ³⁰ erg s ^{–1}	2.1 \times 10 ²⁹ erg s ^{–1}
Imaging timescale	10 s	2 s
Epoch	October 2022 to February 2023	February 2023 to August 2023
Dispersion measure, DM	–	145.8 \pm 3.5 pc cm ^{–3}
Right ascension (J2000)	19h 35min 05.175 s \pm 0.3"	
Declination (J2000)	+21° 48' 41.504" \pm 0.6"	
Period	3,225.309 \pm 0.002 s	
Period derivative	\leq (1.2 \pm 1.5) \times 10 ^{–10} s s ^{–1}	
Distance (YMW16), d_1	4.3 kpc	
Distance (NE2001), d_2	5.4 kpc	
Neutron-star surface dipole magnetic-field strength	\leq a few \times 10 ¹⁶ G	
White-dwarf surface dipole magnetic-field strength	\leq a few \times 10 ¹⁰ G	
Spin-down luminosity (white dwarf), \dot{E}	\leq 1.4 \times 10 ³¹ erg s ^{–1}	
Spin-down luminosity (neutron star), \dot{E}	\leq 1.4 \times 10 ²⁶ erg s ^{–1}	

Uncertainties are 1 σ errors on the last significant quoted digit. The best-fit coordinates in the table are from the MeerKAT localization and the quoted beamformed time resolution corresponds to the best time resolution of all the backend instruments used (see Methods for more details).

In the second scenario, it is likely that there are different emission modes at play. The source was undetectable with ASKAP in all follow-up observations post 5 November 2022, until the first MeerKAT observation on 3 February 2023 with its five times better sensitivity. The MeerKAT pulses that would have been undetectable at ASKAP are analogous to the ‘quiet’ pulse mode in PSR B0823+26, and the ‘dwarf pulse’ mode in PSR B2111+46⁸. The pulses in these modes are generally undetectable in lower-sensitivity and/or low time-resolution observations such as with ASKAP. These weak pulses potentially exist between the nulling or quenched states of ASKAP J1935+2148. The location of the source at the edge of the supernova remnant in Extended Data Fig. 2 makes it difficult to determine exactly what background emission to subtract. Therefore, we are unable to confirm the presence of persistent continuum radio emission that might be indicative of a wind nebula in either the MeerKAT or ASKAP data (Methods).

Collectively, the pulse widths, spectra and polarization properties of the ASKAP and MeerKAT detections suggest different physical coherent processes even though they occur at roughly the same

rotational phase. Coherent radio emission from rotating neutron stars is efficiently generated by the creation of electron–positron pairs in the magnetosphere. The rotational spin-down creates an electric potential at the polar cap, causing pair production. Such charged plasma can emit radio waves that can be attributed to curvature radiation and inverse Compton scattering, and diverse magnetic-field configurations in emission models, including dipolar, multipolar and twisted fields along with vacuum gaps and space-charge-limited flows^{9,10}. Magnetically powered neutron stars, however, generate coherent radio emission through decaying magnetic fields¹¹. Extended Data Fig. 3 shows the manifestation of the physics underlying coherent and incoherent emitters, and indicates a coherent emission mechanism (brightness temperatures between 10¹⁴ K and 10¹⁶ K) being responsible for both the ASKAP and MeerKAT detections of ASKAP J1935+2148.

When comparing with other known long-period sources, ASKAP J1935+2148 appears to be similar to GLEAM-X J162759.5–523504.3¹² and GPM J1839–10¹³ albeit with a period that is four times longer but with a duty cycle not too dissimilar. GLEAM-X J162759.5–523504.3 was active for only three months, while GPM J1839–10 has remained active for over three decades^{12,13}. Despite searches across radio data from the Giant Metrewave Radio Telescope (GMRT), Very Large Array (VLA) and VLA Low-band Ionosphere and Transient Experiment (VLITE) spanning 2013 to 2023, no pulses from ASKAP J1935+2148 were detected. We note that ASKAP J1935+2148 shares similarities with the Galactic Centre radio transient (GCRT), or ‘Burper’, GCRT J1745–3009. At the time of its discovery, GCRT J1745–3009 showed 10-min-wide pulses with a periodicity of 77 min (ref. 14), but subsequent observations revealed narrower and weaker pulses spanning 2 min (ref. 15). Varying circular polarization was also found in one of the pulses¹⁶. The similarities in the periods and the different emission states imply that ASKAP J1935+2148 could be a bridge between GCRT J1745–3009, GLEAM-X J162759.5–523504.3 and GPM J1839–10.

Owing to the proximity of SGR 1935+2154, there are numerous archival high-sensitivity X-ray observations at the position of ASKAP J1935+2148 (Methods and Extended Data Table 2). We focused on observations with the Chandra X-ray Observatory and Neil Gehrels Swift Observatory¹⁷. Using a combination of the more sensitive Chandra observations, we did not detect any X-ray source at the location of ASKAP J1935+2148. For an average DM inferred distance of 4.85 kpc (Table 1), this corresponds to a luminosity limit of about $4 \times 10^{30} d_{4.85}^2$ erg s^{–1} (Methods) for a blackbody spectral model and a power-law spectral model for non-thermal emission from a neutron star. This is below the X-ray luminosities of most but not all rotation-powered pulsars and magnetars^{18,19} and is comparable to the X-ray luminosities of other long-period radio transients ($\leq 10^{32-33}$ erg s^{–1})^{12,13}. We also searched for flaring activity in ASKAP J1935+2148 using Swift, with 291 individual visits using the X-ray Telescope²⁰ lasting 5–2,600 s from December 2010 to December 2022 for a total exposure time of 302.4 ks (exposure corrected). We see no sources in the summed dataset at the position of ASKAP J1935+2148 (Methods). The repeated visits with Swift allow us to rule out any flaring behaviour during this period.

Archival 300 s exposures in the J, H and K_s bands (1.2 μ m, 1.6 μ m and 2.1 μ m) with the Very Large Telescope (VLT) using the near-infrared HAWK-I²¹ imager showed a source within the conservative 1.5" ASKAP error radius of ASKAP J1935+2148 (Fig. 3). This source with $J = 18.4 \pm 0.1$ mag, $H = 17.3 \pm 0.1$ mag and $K_s = 17.1 \pm 0.1$ mag (Vega) is catalogued as PSO J293.7711+21.8119 in Data Release 2 of the Pan-STARRS1 (Panoramic Survey Telescope and Rapid Response System; PS1) 3 π survey²². We compute the chance of finding a source randomly (drawn from the background) in the K_s image, which has the highest source density, with magnitude brighter than or equal to this value to be 5% (that is $\sim 2\sigma$ association) given the crowded nature of the field. However, to confidently rule out the association, we obtained a spectrum of PSO J293.7711+21.8119 in the 3,200–10,000 Å wavelength range with the

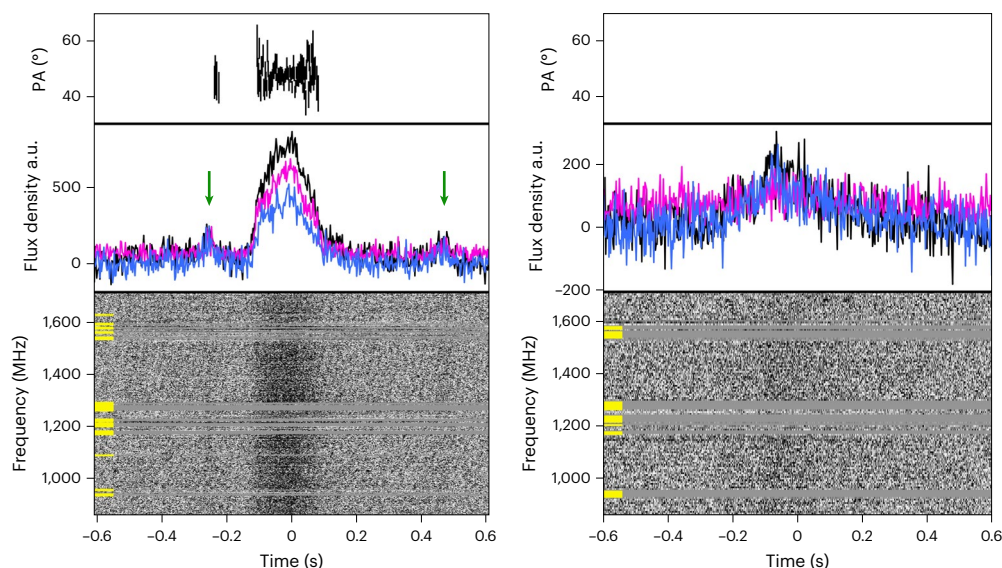


Fig. 2 | The dynamic spectra and polarization pulse profiles of ASKAP J1935+2148 from the MeerKAT beamformed data. Left: a bright detection on 3 February 2023. Right: a weaker detection on 8 May 2023. The data have a time resolution of 2.4 ms and are de-dispersed to a DM of 145.8 pc cm^{-3} and corrected for an RM of $+159.3 \text{ rad m}^{-2}$. Top: the polarization position angle (PA; for values of linear polarization greater than three times the off-pulse noise), which is observed to be flat across the main pulse profile in the left panel. The insufficient signal-to-noise ratio during the detection on 8 May 2023 prevented

robust measurements of polarization position angles. Middle: the Stokes parameter pulse profiles for ASKAP J1935+2148 at 1,284 MHz where black represents the total intensity, magenta represents linear polarization and blue represents circular polarization. The flux density is in arbitrary units as the data are not flux calibrated. The arrows indicate the positions of the pre- and post-cursor bursts for the detection on 3 February 2023 (left). Bottom: the dynamic spectra where the backwards sweeping striations across the observing band in the left panel correspond to $\sim 50 \text{ Hz}$ radio-frequency interference.

Low Resolution Imaging Spectrometer at the Keck telescope in Hawaii (Extended Data Fig. 4). The calibrated spectrum is a red continuum devoid of discernible emission or absorption lines. The combination of the VLT magnitudes and the spectral characteristics suggests that it is an L/T-dwarf star. Gaia Data Release 1 parallaxes for known L and T dwarfs give J-band absolute magnitudes M_J in the range $10 < M_J < 16$ (ref. 23), which implies a distance of less than 0.5 kpc for an apparent magnitude of $J = 18.4$. Because at 4.85 kpc such a star would be undetectable, we conclude that PSO J293.7711+21.8119 is a foreground star that is unlikely to be associated with ASKAP J1935+2148.

The observed period and emission of ASKAP J1935+2148 could be explained by a rotating magnetic white dwarf (MWD) emitting coherent radio emission like a neutron-star pulsar²⁴. MWDs can be either isolated or in interacting binaries. There are ~ 600 known isolated MWDs with surface dipole magnetic fields up to 10^9 G and ~ 200 in interacting binaries with magnetic fields up to a few 10^8 G (ref. 25). Although radio emission from isolated MWDs has never been detected, despite searches for possible counterparts in large-area radio surveys (for example, refs. 26,27), we now entertain this possibility and derive the parameters that would be required to explain the radio emission of ASKAP J1935+2148. If ASKAP J1935+2148 is an isolated rotation-powered MWD, the measured P and upper limit on \dot{P} would yield a surface magnetic-field strength and spin-down luminosity of a few 10^{10} G and a few $10^{31} \text{ erg s}^{-1}$, respectively, for a dipolar magnetic-field configuration, a magnetic inclination angle of 90° and a moment of inertia of 10^{50} g cm^2 . Even though the currently known isolated MWDs have magnetic fields below 10^9 G , it is theoretically possible for MWDs to have surface fields of up to a few 10^{13} G (refs. 28,29). In this case, ASKAP J1935+2148 would be the first MWD discovered to possess such a high magnetic field.

The radius of the source can be related to rotational period and magnetic-field strength to estimate the minimum radius of the source³⁰ (Methods and Extended Data Fig. 5). Even under the most conservative assumptions, we can rule out an isolated MWD origin if we presume that the magnetic field cannot exceed 10^9 G , which is the maximum

measured in an MWD. Similar considerations can also be applied to GLEAM-X J162759.5–523504.3 and GPM J1839–10, and we conclude that it is highly unlikely that the radio emission from these sources can be interpreted in terms of an isolated rotation-powered MWD. However, coherent and highly polarized radio emission has been detected in cataclysmic variables^{26,31}, which are close binary systems containing a white dwarf primary accreting matter from a low-mass M-dwarf companion. In all detection cases, the radio emission appears to arise from the lower corona of the magnetically active M-dwarf and is attributed to the electron cyclotron maser instability. The problem here is that the radio luminosities of cataclysmic variables, in the range 10^{21} – $10^{25} \text{ erg s}^{-1}$ (ref. 26), would be too low to explain the emission of ASKAP J1935+2148. Hence, it is also highly unlikely that a cataclysmic variable could be responsible for the radio emission of ASKAP J1935+2148.

Assuming a neutron-star origin, the period and upper limit on the period derivative correspond to a surface magnetic-field strength and spin-down luminosity of a few 10^{16} G and a few $10^{26} \text{ erg s}^{-1}$, respectively, for a dipolar magnetic-field configuration, a magnetic inclination angle of 90° and a moment of inertia of 10^{45} g cm^2 . It is unclear why a neutron-star magnetar would still possess such a large magnetic field at this stage of its evolution, but explanations have been provided either in terms of the magnetic field's structure (for example, refs. 32,33) or as due to a fall-back accretion disk (for example, ref. 34). Similar to GLEAM-X J162759.5–523504.3¹² and GPM J1839–10¹³, the observed radio luminosity of ASKAP J1935+2148 is much larger than the inferred spin-down luminosity, suggesting that alternative emission mechanisms must be involved to explain the radio emission of these long-period radio transients.

Achieving the observed duty cycle of approximately $\sim 1\%$ in ASKAP J1935+2148 necessitates a high degree of beaming, implying the generation and acceleration of relativistic particles—a phenomenon that is generally more easily accommodated in neutron stars than in white dwarfs. Remarkably, the isolated intermittent pulsar PSR J1107–5907, with $P \approx 253 \text{ ms}$, shows the same three distinct emission states as ASKAP J1935+2148³⁵. The emission in both PSR J1107–5907 and

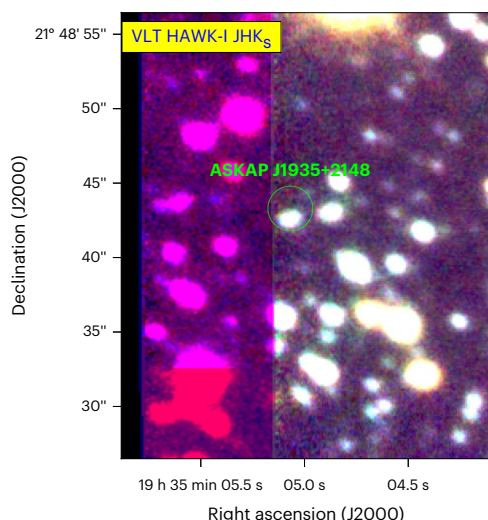


Fig. 3 | Three-colour near-infrared image of the field around ASKAP J1935+2148, from VLT/HAWK-I JHK_s imaging on 2 April 2015. The image cut-out is $20'' \times 30''$. The uncertainty in the position of ASKAP J1935+2148 is shown by a green circle of radius $1.5''$.

ASKAP J1935+2148 alternates between distinct modes, each characterized by unique pulse profiles, polarization properties and, at times, varying intensities. The intricate interplay of magnetic fields, plasma flows and the magnetospheric environment leads to the emergence of these different modes³⁶. Instabilities within the pulsar magnetosphere may trigger transitions between these modes, contributing to the observed switching phenomenon. In addition, changes in the geometry of the magnetic-field configuration and the location of emission sites within the magnetosphere could influence the emitted radiation characteristics. Notably, PSR J1107–5907 is close to the pulsar death line(s)^{37,38} (Extended Data Fig. 1), beyond which radio emission is expected to cease. All these similarities seem to suggest that a neutron-star-like emission mechanism is at play for ASKAP J1935+2148.

In summary, we report the discovery of the long-period source ASKAP J1935+2148, which is unique compared with other known long-period sources, by manifesting three distinctive emission states reminiscent of mode-switching pulsars. The strong pulse mode shows bright and linearly polarized pulses lasting tens of seconds, the weak pulse mode features faint and circularly polarized pulses lasting hundreds of milliseconds, and the completely nulling or quiescent mode shows an absence of pulses. These diverse emission states offer valuable insights into the magnetospheric processes and emission mechanisms at play within this object, with similarities to the radio pulsars PSR J1107–5907, PSR B0823+26 and PSR B2111+46. Given the brief 3-month activity of GLEAM-X J162759.5–523504.3, ongoing monitoring may unveil emission modes similar to the those observed in ASKAP J1935+2148. We see that radio emission via pair production within dipolar magnetospheres presents considerable challenges²⁴. However, a large magnetic field can power the observed radio emission via the dissipation of energy due to magnetic re-connection events, higher-order magnetic fields and untwisting of field lines due to plastic motion of the crust^{39,40}. It would be prudent to study further whether such processes can persist for long timescales consistent with the long-term emission seen in a few long-period sources. Population-synthesis simulations incorporating various parameters such as masses, radii, beaming fractions and magnetic field show that only a limited number of long-period radio emitters of neutron-star origins are expected to exist in the Galaxy²⁴. Conversely, in the white-dwarf scenario, a sizable population of long-period emitters can be accounted for. Nonetheless, explaining the production of coherent radio emission remains a formidable task in either scenario^{24,41}. While MWDs have been

considered to be responsible for the radio emission observed in sources such as GLEAM-X J162759.5–523504.3 and GPM J1839–10, we have ruled out this possibility for ASKAP J1935+2148. Thus, it is much more likely for ASKAP J1935+2148 to be an ultralong period magnetar or neutron star either isolated or in a binary system. Continued monitoring of this source should allow us to determine whether additional periods are present and the possible existence of a companion star.

Methods

ASKAP

The ASKAP array comprises 36 antennas, each equipped with a prime-focus phased array feed (PAF). Each PAF has 188 linearly polarized receiving elements sensitive to frequencies between 0.7 GHz and 1.8 GHz. The signal from each element is channelized to 1 MHz frequency resolution over a usable bandwidth of 288 MHz. The standard ASKAP hardware correlator produces visibilities on a 10 s timescale. During the detection of ASKAP J1935+2148, ASKAP was operated in the square 6×6 configuration with 1.05° pitch and 887.5 MHz central frequency. The pointing centre was chosen such that ASKAP's large field of view ($\sim 30 \text{ deg}^2$) would also encompass the magnetar SGR 1935+2154 known to have produced a burst with fast radio burst like (FRB) energies in 2020^{42,43} and several less energetic bursts since.

The source was found during testing of a fast pulse-detection pipeline. The pipeline subtracts visibilities from neighbouring 10 s integrations and then images the result. The process effectively subtracts out quiescent emission from the field and retains only sources that change dramatically over a single integration. As such sources are rare, most images are effectively dominated by thermal noise and so do not require computationally expensive deconvolution. Once the image is checked for peaks above the noise, it is discarded to minimize storage requirements. The process is repeated for all time integrations and all 36 ASKAP beams. The processing initially found no detections in the first epoch of the ASKAP observation but found a bright pulse in beams 21, 22 and 23 of the second ASKAP epoch.

While the pulse-detection pipeline is reasonably effective for finding bright pulses, it forgoes some sensitivity to weak pulses to minimize resource usage. Once we had discovered ASKAP J1935+2148, more traditional techniques were used to investigate the pulse. A deep model image was derived for the beam and subtracted from the visibility data. The data were then phase shifted to the location of the source and dynamic spectra extracted (averaging over all baselines $>200.0 \text{ m}$). This allowed weaker pulses to be detected and also allowed the linear polarization properties to be analysed. This approach was also repeated for MeerKAT observations.

Murriyang

The shortest ASKAP imaging observation (SBID 44918 in Extended Data Table 1), took place at the same time the 64 m Parkes (Murriyang) radio telescope was pointed at the known radio-burst emitting magnetar SGR 1935+2154. This observation was taken using the Ultra Wideband Low receiver system, spanning a bandwidth of 704–4,032 MHz. The position of ASKAP J1935+2148 was well within the 30-arcmin-wide low-frequency part of the Ultra Wideband Low beam. Only one weak pulse ($\sim 9\sigma$ or 10.7 mJy per beam) was detected from ASKAP J1935+2148 in the ASKAP data but no detection was made in the Parkes data above a signal-to-noise ratio of 8.

MeerKAT

In the observations presented in this work, MeerKAT operated at the L band (0.86–1.71 GHz) in the c856M4k configuration where the correlations were integrated for 2 s before saving to disk. We used PKS J1939–6342 as the primary flux calibrator and bandpass calibrator, and PKS J2011–0644 as the phase calibrator. MeerKAT was also used to simultaneously perform beamformed observations in the incoherent and coherent modes using MeerTRAP. The MeerTRAP backend is the

combination of two systems: the Filterbank and Beamforming User Supplied Equipment (FBFUSE), a multiple-beam beamformer^{44,45}, and the Transient User Supplied Equipment (TUSE), a real-time transient detection instrument⁴⁶. FBFUSE applies the geometric and phase delays (obtained by observing a bright calibrator) before combining the data streams from the dishes into 1 incoherent beam and up to 780 coherent beams recording in total intensity, only. The beams can be placed at any desired location within the primary beam of the array, but are by default tessellated into a circular tiling centred on the boresight position, and spaced so that the response patterns of neighbouring beams intersect at the 25% peak power point. The beams are then sent over the network to TUSE for processing.

The TUSE single-pulse search pipeline searches for total intensity pulses in real time at a sampling time of 306.24 μ s, up to a maximum boxcar width of 140 ms in the dispersion measure range of 0–5118.4 pc cm⁻³ at the L band. Only extracted candidate files are saved to disk for further investigation. Further details on the MeerTRAP backend can be found in refs. 47,48. The Accelerated Pulsar Search User Supply Equipment (APSUSE) backend instrument was used to record total intensity data with 4,096 frequency channels. In addition, full polarization data for the on-source beam were recorded to disk, but not searched in real time, using the Pulsar Timing User Supplied Equipment (PTUSE) backend of the MeerKAT pulsar timing project MeerTime described in ref. 49. These data were recorded in the PTUSE search mode with a sampling time of 38.28 μ s in the psrfits format.

To address the impact of baseline variation in the recorded data, we utilized the APSUSE off-source beam as a reference to eliminate the baseline of the on-source beam. Following this process, we conducted a search for single pulses using TransientX (<https://github.com/ypmen/TransientX>)⁵⁰, within a DM range of 120–160 pc cm⁻³ and a maximum pulse width of 1 s. This search yielded the detection of the two pulses in the PTUSE data. Subsequently, we extracted the polarization profiles from the PTUSE data of these two pulses, having removed the baseline based on the off-source APSUSE beam.

Period estimation

We generated ToAs for each of the detections made with the ASKAP and MeerKAT observation in Extended Data Table 1. Manipulation of the data used the tools available in the PSRCHIVE package⁵¹. The ToAs for the ASKAP detections are chosen to be the midpoints of the 10 s integrations they were detected in, with the error on the ToA equal to the duration of a non-detection in 10 s integrations immediately preceding, and succeeding the first and last detections of a pulse, respectively. The MeerKAT ToAs were obtained by using PSRCHIVE's PAT on the beamformed data to estimate the time of the peak flux. Given the variability in the morphology of individual pulses, and presumable jitter in the emission measuring the pulse arrival times, we estimate the uncertainty on the arrival times to be the half-width at half-maximum of the widths of the pulses. The initial timing analysis for both telescopes used the best known period and DM at the time and the position determined from the imaging.

Timing was done using TEMPO2⁵² with the JPL DE436 planetary ephemeris (<https://naif.jpl.nasa.gov/pub/naif/JUNO/kernels/spk/de436s.bsp.lbl>). The ToAs were fitted using a model including the period P and period derivative \dot{P} . We do not need to fit for position as it is well determined from the imaging as described in previous sections. We also do not fit for DM as this is sufficiently well determined from optimizing the signal to noise of the individual MeerKAT pulses.

Archival radio searches

VLITE. The VLITE^{53,54} is a commensal instrument on the National Radio Astronomy Observatory's Karl G. Jansky Very Large Array that records and correlates data across a 64 MHz bandwidth at a central frequency of 340 MHz. Since 20 July 2017, VLITE has been operating on up to

18 antennas during nearly all regular VLA operations, accumulating roughly 6,000 h of data per year. An automated calibration and imaging pipeline⁵⁵ processes all VLITE data, producing final calibrated visibility datasets and self-calibrated images. These images and associated META data are then passed through the VLITE Database Pipeline⁵⁵ to populate a Structured Query Language database containing catalogued sources.

Using the VLITE Database Pipeline, we searched for all VLITE datasets that contain the position of ASKAP J1935+2148 within 2.5° from the phase centre of the VLITE observations taken when the VLA was in its A and B configurations. We note that the half-power radius of the VLITE primary-beam response is $\sim 1.25^\circ$; however, the system is sensitive to sources well beyond this radius. We identified 124 VLITE datasets observed between 9 November 2017 and 22 August 2023. From these, we selected all observations with a length of at least 15 min, for a total of 26 observations in A configuration (angular resolution $\sim 5''$) and 10 observations in B configuration (resolution $\sim 20''$). None of these 36 datasets are targeted observations of ASKAP J1935+2148, rather the source position ranges between a radius of 1.1° to 2.2° from the pointing centre of the VLITE observation.

To search for possible 340 MHz emission from ASKAP J1935+2148 in the VLITE data, we first subtracted all known continuum sources from the self-calibrated visibilities of each observation, we then phase shifted the data to the position of ASKAP J1935+2148 using *chgcentre*⁵⁶, and finally we made a time series of dirty images of the target at 10 s and 4 s intervals using WSClean⁵⁶. The primary-beam corrected noise in the 10 s snapshots ranges on average from 41 mJy per beam (when the position of ASKAP J1935+2148 is 1.1° away from the VLITE phase centre) to 130 mJy per beam (at 2.2°). In the 4 s snapshots, the average primary-beam corrected noise ranges between 62 mJy per beam (at 1.1° from the phase centre) and 181 mJy per beam (at 2.2°). No obvious pulses from ASKAP J1935+2148 were detected.

VLA and GMRT. The archives of the VLA and the GMRT were searched for data in which the position of ASKAP J1935+2148 lies within the observation field of view. VLA P-band (~ 325 MHz) observations of PSR 1937+21, 1.1° away, were made on 25 September 2013, 28/29 November 2013, 30 November/1 December 2013, 1/2 December 2013 and 7 July 2014 with the array in the B and A configurations ($\sim 20''$ and $\sim 5''$ resolutions), respectively. The 25 September 2013 observation was on-source for 42 min except for short calibrator scans intermixed, while the other 2013 observations consisted of three 6 min scans separated by 1 h, and the 2014 observation consisted of ten 6 min scans spread over 4 h. Calibration and imaging were performed using the Astronomical Imaging Processing System (AIPS)⁵⁷. Amplitude and phase calibrations were both performed using 3C48, as no separate phase calibrator was observed. Imaging was performed with the AIPS task, IMAGR. The field was self-calibrated on a wide-field image using 19 facets to cover the $\sim 3^\circ$ (full-width at half-maximum) field of view. Ten-second integration snapshot images were made after subtracting the deep image clean components from the UV data using the AIPS task, UVSUB. The root mean square (RMS) noise of the 10 s snapshot images at the location of ASKAP J1935+2148 was typically ~ 15 mJy per beam after applying a $1.5\times$ correction for primary-beam attenuation.

Two L-band (~ 1.4 GHz) observations on 28–29 May 2020 (GMRT; 2.5 h; $\sim 2''$ resolution) and 27 June 2021 (VLA; 1 h; C configuration; $\sim 10''$ resolution) targeted SGR 1935+2154 located only 0.1° away from ASKAP J1935+2148. A similar analysis in AIPS was followed as with the P-band observations except that wide-field imaging was not necessary due to the much smaller $\sim 0.5^\circ$ (full-width at half-maximum) fields of view. The amplitude and phase calibrators were 3C48 and 1822-096 (GMRT) and 3C286 and J1925+2106 (VLA). The RMS noise of the 5.4 s (GMRT) and 5.0 s (VLA) snapshot images at the location of ASKAP J1935+2148 were both typically ~ 0.5 mJy per beam after applying a $1.1\times$ correction for primary-beam attenuation. No obvious pulses from ASKAP J1935+2148 were detected.

X-ray searches

For Chandra, we identified 5 Chandra observations for a total of 157.7 ks of exposure as listed in Extended Data Table 2. For all observations, ASKAP J1935+2148 was located on a front-illuminated charge-coupled device (CCD): ACIS-S2 for 21305/21306 and ACIS-S4 for the remainder.

The observations were analysed and combined using CIAO version 4.15.1, with CALDB 4.10.2³⁸. We first examined all observations individually for background flares by looking visually at the summed light curves. No flares were identified. We reprocessed the data to level 2 using a consistent calibration database, and reprojected the data to a common tangent point. We then combined the reprojected observations to create an exposure-corrected image. No source was found within 2" of ASKAP J1935+2148. We also looked at the individual reprojected event files. For each file we computed the number of events within a 2" radius of ASKAP J1935+2148 along with the background rate determined from all of the counts on the appropriate CCD between 0.3 keV and 10 keV. A total of 6 counts were found near the position of ASKAP J1935+2148, but the mean background rate predicts 3.8 counts, and the chance of getting ≥ 6 counts is 9.2%. Therefore, we do not consider this a detection and place a 3σ upper limit of 10 counts in 157.7 ks or a count-rate limit of 6.3×10^{-5} counts per second (0.3–10 keV).

On the basis of the observed DM of 145.8 ± 3.5 pc cm⁻³, we predict an absorbing column density of $N_{\text{H}} \approx 4 \times 10^{21}$ cm⁻² (ref. 59). We computed unabsorbed flux limits for two spectral models: a blackbody with $kT = 0.3$ keV (appropriate for thermal emission from a young pulsar/magnetar), and a power law with index $\Gamma = 2$ (appropriate for non-thermal emission from an energetic pulsar/magnetar), following ref. 34. This was done using PIMMS (<https://cxc.harvard.edu/toolkit/pimms.jsp>), where we assumed a response appropriate for Chandra cycle 22 and used the ACIS-I CCDs in place of the front-illuminated ACIS-S CCDs. With the blackbody model, we infer an unabsorbed flux limit of $F_{\text{BB}} < 1.3 \times 10^{-15}$ erg s⁻¹ cm⁻², while with the power-law model we infer an unabsorbed flux limit of $F_{\text{PL}} < 1.7 \times 10^{-15}$ erg s⁻¹ cm⁻². These imply luminosity limits of about $4 \times 10^{30} d_{4.85}^2$ erg s⁻¹. Overall, the Chandra observations lead to very low limits regarding the time-averaged X-ray flux.

To search for any flaring from ASKAP J1935+2148, we used extensive observations from Swift, with 291 individual visits using the X-ray Telescope²⁰ lasting 5–2,600 s from December 2010 to December 2022 for a total exposure time of 302.4 ks (exposure corrected). We combined the individual barycentred exposures using HEADAS⁶⁰ on SciServer⁶¹ into a single exposure-corrected dataset. We see no sources in the summed dataset at the position of ASKAP J1935+2148: there are 33 counts within 15" of ASKAP J1935+2148, but the background expectation computed using an annulus from 30" to 60" is 35.4 counts, so we estimate a 3σ upper limit of 53.0 counts or a count-rate limit of 1.7×10^{-4} counts per second (0.15–10 keV). Using the same spectral models as above, we limit the unabsorbed flux (0.3–10 keV) to be $F_{\text{BB}} < 7.4 \times 10^{-15}$ erg s⁻¹ cm⁻² and $F_{\text{PL}} < 1.1 \times 10^{-14}$ erg s⁻¹ cm⁻². These are much less constraining than the corresponding Chandra limits.

Optical and near-infrared searches

The position of ASKAP J1935+2148 was observed by the VLT using the near-infrared HAWK-I²¹ imager. There were a number of observations of SGR 1935+2154 that placed ASKAP J1935+2148 near the edge of the field of view; we found the observations on 2 April 2015 to be the most useful. These included 300 s exposures in the J, H and K_s bands (1.2 μ m, 1.6 μ m and 2.1 μ m). However, even these exposures were not ideal, with weight-map values only 20% of the peak at the position of ASKAP J1935+2148. Nonetheless, the collecting area of VLT makes them valuable.

We show a RGB composite of the field around ASKAP J1935+2148 in Fig. 3. It is clear that the source is near the edge of the field, and is barely covered by the H-band image. Coverage in the J and K_s bands is better. There is a source within a 1.5" radius around ASKAP J1935+2148 and has $J = 18.4 \pm 0.1$ mag, $H = 17.3 \pm 0.1$ mag and $K_s = 17.1 \pm 0.1$ mag (Vega). We compute the chance of finding a source randomly (drawn

from the background) in the K_s image with magnitude brighter than or equal to this value is 5% (that is, $\sim 2\sigma$ association). This suggests that the association between the near-infrared source and ASKAP J1935+2148 is not statistically significant. Otherwise, we infer 5σ upper limits of $J > 21.4$ mag, $H > 20.5$ mag and $K_s > 19.8$ mag. Aside from the deep VLT pointings, we examined images from Data Release 2 of the PS1 3 π survey²². There is a source in the 'stack' catalogue that corresponds to the near-infrared source identified above. This source is catalogued as PSO J293.7711+21.8119. The source is not detected in the g, r or i bands, and has detections only in z (22.0 ± 0.3 mag) and y (20.4 ± 0.1). For the other bands and for the rest of the error region, we adopt the standard PS1 stack upper limits $g > 23.3$, $r > 23.2$, $i > 23.1$, $z > 22.3$ and $y > 21.3$.

Search for persistent radio emission

To ascertain whether there is an unpulsed radio component that might be attributed to a wind nebula, or perhaps indicate emission of a non-neutron-star origin, we imaged the ASKAP visibility data. In a stacked ASKAP deep image at 887.5 MHz, if we subtract the mean background emission, there is no detection above 3σ with an RMS of 25 μ Jy per beam. However, the location of the source at the edge of the supernova remnant in Extended Data Fig. 2 makes it difficult to determine exactly what background emission to subtract. Therefore, we are unable to confirm the presence of potential (possibly faint) persistent continuum radio emission in either the MeerKAT or ASKAP data.

Faraday conversion

We tested whether the large circular polarization fraction seen in the MeerKAT beamformed data could be due to Faraday conversion using a simple phenomenological model⁶², where the polarization vector is modelled as a series of frequency-dependent rotations on the Poincaré sphere. However, we failed to recover any notable frequency dependence to the circular polarization. This indicates that it is either intrinsic to the emission mechanism or arises from a more complex propagation effect such as the partially coherent addition of linearly polarized modes⁶³.

Model constraints

White dwarf. We examine the potential for the optical/near-infrared data described above to constrain white-dwarf scenarios for the source. We used the synthetic photometry (see <https://www.astro.umontreal.ca/~bergeron/CoolingModels/>) of refs. 64–66 together with the three-dimensional extinction model of ref. 67 to compute distance constraints as a function of effective temperature for hydrogen-atmosphere (DA) white dwarfs with masses 0.6 M_{\odot} and 1.0 M_{\odot} , representing standard and massive white dwarfs, respectively (using helium-atmosphere DB white dwarfs does not change the conclusions). We did two analyses, one where we modelled the potential near-infrared counterpart and one where we treated the source as non-detections. Note that there are large degeneracies involved: extinction and effective temperature are highly degenerate, and other quantities such as mass (and hence radius) degenerate with distance. When considering the potential near-infrared counterpart as correct, and given the sparse data that would all be on the Rayleigh–Jeans tail, we unsurprisingly found a plausible fit to the VLT data with effective temperature, $T_{\text{eff}} \approx 15,000$ K and distance ~ 6 kpc (implying reddening $E(B - V) \approx 2.8$). However, the implied radius is $\sim 0.8 R_{\odot}$, leading us to conclude that this source cannot be expected by standard white-dwarf models.

Considering only upper limits (so assuming that the source PSO J293.7711+21.8119 is not associated with ASKAP J1935+2148), we find that a white dwarf with $T_{\text{eff}} < 30,000$ K could be present at distances > 1 kpc. Despite their greater sensitivity, we found the VLT data generally less constraining than the PS1 data given the range of effective temperatures considered. Given the implied average DM distance of 4.85 kpc from the NE2001 and YMW16 models, we do not consider the limits described here especially constraining. Under the framework of

coherent radio emission from pair production, the compactness of the source can be related to the period and magnetic field so that we can estimate the minimum radius of the source³⁰ using

$$R \gtrsim 4 \times 10^9 \left(\frac{Q_c}{10} \right)^{4/17} \left(\frac{P}{1,000 \text{ s}} \right)^{13/17} \left(\frac{B}{10^9 \text{ G}} \right)^{-8/17} \text{ cm}, \quad (1)$$

where P is the period in seconds, B is the magnetic field in gauss and $Q_c = \rho_c/R$ is the dimensionless characteristic field curvature radius in which the curvature radius near the polar cap is assumed to be $\rho_c \approx 10R$. The conventional emission model for any compact object to emit dipole radiation assumes the existence of a vacuum gap above the polar cap. To sustain pair production, the potential difference across this gap must be sufficiently large and this is no longer possible beyond the classic death line³⁷. As a result, pair production and consequently, radio emission ceases. The relation above therefore encodes radio death-line physics due to requirements on pair-cascade production and provides a lower limit on the compactness of an object to sustain this emission. A choice of $Q_c \gg 10$ is commensurate with the expected small polar cap size for a $P \approx 1,000$ s rotator. Assuming $10 \leq Q_c \leq 10^5$ and $B = 10^9$ G, we can rule out an isolated magnetic white-dwarf origin for the observed emission as the estimated lower limit on the radius of $0.14 R_\odot$, even in the case of $Q_c = 10$, is much too large for a white dwarf (Extended Data Fig. 5).

Neutron star. It has been proposed that bright coherent radio bursts can be produced by highly magnetized neutron stars that have attained long rotation periods (few tens to a few thousands of seconds), called ultralong period magnetars. Typically, magnetars have quiescent X-ray luminosities anywhere between $10^{31} \text{ erg s}^{-1}$ and $10^{36} \text{ erg s}^{-1}$ (refs. 19,68) regardless of radio emission (typically they are brighter in X-rays following outbursts that lead to radio emission), and so our deep X-ray limits from searching archival X-ray data challenge the magnetar interpretation. However, there are subclasses of magnetars with considerably weaker X-ray emission, $<10^{30} \text{ erg s}^{-1}$, such as the ‘low field’ magnetars whose⁶⁹ spin-down inferred fields are $\sim 10^{13}$ G, but where local X-ray absorption features suggest much higher localized fields^{70,71}. If indeed ASKAP J1935+2148 and similar sources are part of another emerging subclass of magnetars, the quiescent X-ray luminosities (which are attributed to the decay of large-scale dipole magnetic fields) may be lower. If that is the case, it would also explain the location of ASKAP J1935+2148 as magnetars are typically expected to be young objects that lie in the Galactic Plane¹¹. Combining all these observational aspects, ASKAP J1935+2148, is probably part of an older population of magnetars with long spin periods and low X-ray luminosities, but magnetized enough to be able to produce coherent radio emission. It is important that we probe this hitherto unexplored region of the neutron-star parameter space to get a complete picture of the evolution of neutron stars, and this may an important source to do so.

Data availability

The data that support the findings of this study are available on Zenodo at <https://doi.org/10.5281/zenodo.10989868> (ref. 72).

Code availability

The timing was performed using TEMPO2 (ref. 52). Specific Python scripts used in the data analysis are available on request from M.C.

References

- Brentjens, M. A. & de Bruyn, A. G. Faraday rotation measure synthesis. *Astron. Astrophys.* **441**, 1217–1228 (2005).
- Zhu, W. et al. A radio pulsar phase from SGR J1935+2154 provides clues to the magnetar FRB mechanism. *Sci. Adv.* **9**, ead6198 (2023).
- Oppermann, N. et al. An improved map of the Galactic Faraday sky. *Astron. Astrophys.* **542**, A93 (2012).
- Cordes, J. M. & Lazio, T. J. W. NE2001.I. A new model for the galactic distribution of free electrons and its fluctuations. Preprint at <https://arxiv.org/abs/astro-ph/0207156> (2002).
- Yao, J. M., Manchester, R. N. & Wang, N. A new electron-density model for estimation of pulsar and FRB distances. *Astrophys. J.* **835**, 29 (2017).
- Lower, M. E., Johnston, S., Shannon, R. M., Bailes, M. & Camilo, F. The dynamic magnetosphere of Swift J1818.0–1607. *Mon. Not. R. Astron. Soc.* **502**, 127–139 (2021).
- Basu, R., Mitra, D. & Melikidze, G. I. Spectral variation across pulsar profile due to coherent curvature radiation. *Astrophys. J.* **927**, 208 (2022).
- Chen, X. et al. Strong and weak pulsar radio emission due to thunderstorms and raindrops of particles in the magnetosphere. *Nat. Astron.* **7**, 1235–1244 (2023).
- Ruderman, M. A. & Sutherland, P. G. Theory of pulsars: polar gaps, sparks, and coherent microwave radiation. *Astrophys. J.* **196**, 51–72 (1975).
- Zhang, B., Gil, J. & Dyks, J. On the origins of part-time radio pulsars. *Mon. Not. R. Astron. Soc.* **374**, 1103–1107 (2007).
- Kaspi, V. M. & Beloborodov, A. M. Magnetars. *Annu. Rev. Astron. Astrophys.* **55**, 261–301 (2017).
- Hurley-Walker, N. et al. A radio transient with unusually slow periodic emission. *Nature* **601**, 526–530 (2022).
- Hurley-Walker, N. et al. A long-period radio transient active for three decades. *Nature* **619**, 487–490 (2023).
- Hyman, S. D. et al. A powerful bursting radio source towards the Galactic Centre. *Nature* **434**, 50–52 (2005).
- Hyman, S. D. et al. A faint, steep-spectrum burst from the radio transient GCRT J1745–3009. *Astrophys. J. Lett.* **660**, L121–L124 (2007).
- Roy, S. et al. Circularly polarized emission from the transient bursting radio source GCRT J1745–3009. *Astrophys. J. Lett.* **712**, L5–L9 (2010).
- Gehrels, N. et al. The Swift Gamma-Ray Burst Mission. *Astrophys. J.* **611**, 1005–1020 (2004).
- Vahdat, A., Posselt, B., Santangelo, A. & Pavlov, G. G. Toward an X-ray inventory of nearby neutron stars. *Astron. Astrophys.* **658**, A95 (2022).
- Olausen, S. A. & Kaspi, V. M. The McGill Magnetar Catalog. *Astrophys. J. Suppl. Ser.* **212**, 6 (2014).
- Burrows, D. N. et al. The Swift X-Ray Telescope. *Space Sci. Rev.* **120**, 165–195 (2005).
- Pirard, J.-F. et al. HAWK-I: A new wide-field 1- to 2.5- μm imager for the VLT. *Proc. SPIE* **5492**, 1763–1772 (2004).
- Chambers, K. C. et al. The Pan-STARRS1 Surveys. Preprint at <https://arxiv.org/abs/1612.05560> (2016).
- Smart, R. L. et al. The Gaia ultracool dwarf sample—I. Known L and T dwarfs and the first Gaia data release. *Mon. Not. R. Astron. Soc.* **469**, 401–415 (2017).
- Rea, N. et al. Long-period radio pulsars: population study in the neutron star and white dwarf rotating dipole scenarios. *Astrophys. J.* **961**, 214 (2024).
- Ferrario, L., Wickramasinghe, D. & Kawka, A. Magnetic fields in isolated and interacting white dwarfs. *Adv. Space Res.* **66**, 1025–1056 (2020).
- Barrett, P., Dieck, C., Beasley, A. J., Mason, P. A. & Singh, K. P. Radio observations of magnetic cataclysmic variables. *Adv. Space Res.* **66**, 1226–1234 (2020).
- Pelisolì, I. et al. A survey for radio emission from white dwarfs in the VLA Sky Survey. Preprint at <https://arxiv.org/abs/2402.11015> (2024).
- Franzon, B. & Schramm, S. Effects of strong magnetic fields and rotation on white dwarf structure. *Phys. Rev. D* **92**, 083006 (2015).

29. Otoniel, E. et al. Strongly magnetized white dwarfs and their instability due to nuclear processes. *Astrophys. J.* **879**, 46 (2019).
30. Beniamini, P. et al. Evidence for an abundant old population of Galactic ultra-long period magnetars and implications for fast radio bursts. *Mon. Not. R. Astron. Soc.* **520**, 1872–1894 (2023).
31. Ridder, M. E., Heinke, C. O., Sivakoff, G. R. & Hughes, A. K. Radio detections of two unusual cataclysmic variables in the VLA Sky Survey. *Mon. Not. R. Astron. Soc.* **519**, 5922–5930 (2023).
32. Pons, J. A. & Geppert, U. Magnetic field dissipation in neutron star crusts: from magnetars to isolated neutron stars. *Astron. Astrophys.* **470**, 303–315 (2007).
33. Ferrario, L. & Wickramasinghe, D. Origin and evolution of magnetars. *Mon. Not. R. Astron. Soc.* **389**, L66–L70 (2008).
34. Rea, N. et al. Constraining the nature of the 18 min periodic radio transient GLEAM-X J162759.5–523504.3 via multiwavelength observations and magneto-thermal simulations. *Astrophys. J.* **940**, 72 (2022).
35. Young, N. J., Weltevrede, P., Stappers, B. W., Lyne, A. G. & Kramer, M. On the apparent nulls and extreme variability of PSR J1107–5907. *Mon. Not. R. Astron. Soc.* **442**, 2519–2533 (2014).
36. Bartel, N., Morris, D., Sieber, W. & Hankins, T. H. The mode-switching phenomenon in pulsars. *Astrophys. J.* **258**, 776–789 (1982).
37. Chen, K. & Ruderman, M. Pulsar death lines and death valley. *Astrophys. J.* **402**, 264 (1993).
38. Zhang, B., Harding, A. K. & Muslimov, A. G. Radio pulsar death line revisited: is PSR J2144–3933 anomalous? *Astrophys. J. Lett.* **531**, L135–L138 (2000).
39. Jones, P. B. Nature of fault planes in solid neutron star matter. *Astrophys. J.* **595**, 342–345 (2003).
40. Lyutikov, M. Magnetar activity mediated by plastic deformations of neutron star crust. *Mon. Not. R. Astron. Soc.* **447**, 1407–1417 (2015).
41. Tong, H. On the nature of long period radio pulsar GPM J1839–10: death line and pulse width. *Res. Astron. Astrophys.* **23**, 125018 (2023).
42. Bochenek, C. D. et al. A fast radio burst associated with a Galactic magnetar. *Nature* **587**, 59–62 (2020).
43. CHIME/FRB Collaboration et al. A bright millisecond-duration radio burst from a Galactic magnetar. *Nature* **587**, 54–58 (2020).
44. Barr, E. D. in *Pulsar Astrophysics the Next Fifty Years* (eds Weltevrede, P. et al.) 175–178 (Cambridge Univ. Press, 2018).
45. Chen, W., Barr, E., Karuppusamy, R., Kramer, M. & Stappers, B. Wide field beamformed observation with MeerKAT. *J. Astron. Instrum.* **10**, 2150013–178 (2021).
46. Caleb, M. et al. Simultaneous multi-telescope observations of FRB 121102. *Mon. Not. R. Astron. Soc.* **496**, 4565–4573 (2020).
47. Rajwade, K. et al. MeerTRAP in the era of multi-messenger astrophysics. *Proc. SPIE* **11447**, 114470J (2020).
48. Caleb, M. et al. Discovery of a radio-emitting neutron star with an ultra-long spin period of 76 s. *Nat. Astron.* **6**, 828–836 (2022).
49. Bailes, M. et al. The MeerKAT telescope as a pulsar facility: system verification and early science results from MeerTime. *Publ. Astron. Soc. Aust.* **37**, e028 (2020).
50. Men, Y. & Barr, E. TransientX: a high-performance single-pulse search package. *Astron. Astrophys.* **683**, A183 (2024).
51. Hotan, A. W., van Straten, W. & Manchester, R. N. PSRCRIVE and PSRFITS: an open approach to radio pulsar data storage and analysis. *Publ. Astron. Soc. Aust.* **21**, 302–309 (2004).
52. Hobbs, G. B., Edwards, R. T. & Manchester, R. N. TEMPO2, a new pulsar-timing package—I. An overview. *Mon. Not. R. Astron. Soc.* **369**, 655–672 (2006).
53. Polisenky, E. et al. Exploring the transient radio sky with VLITE: early results. *Astrophys. J.* **832**, 60 (2016).
54. Clarke, T. E. et al. Commensal low frequency observing on the NRAO VLA: VLITE status and future plans. *Proc. SPIE* **9906**, 99065B (2016).
55. Polisenky, E., Richards, E., Clarke, T., Peters, W. & Kassim, N. The VLITE Database Pipeline. In *Astronomical Data Analysis Software and Systems XXVII* (Astronomical Society of the Pacific Conference Series Vol. 523 (eds Teuben, P. et al.) J441 (Astronomical Society of the Pacific, 2019)).
56. Offringa, A. R. et al. WSCLEAN: an implementation of a fast, generic wide-field imager for radio astronomy. *Mon. Not. R. Astron. Soc.* **444**, 606–619 (2014).
57. Wells, D. C. in *Data Analysis in Astronomy* (Ettore Majorana International Science Series Vol. 2. (eds Gesù, V. D. et al.) 195–209 (Springer, 1985); https://doi.org/10.1007/978-1-4615-9433-8_18
58. Fruscione, A. et al. CIAO: Chandra's data analysis system. *Proc. SPIE* **6270**, 62701V (2006).
59. He, C., Ng, C. Y. & Kaspi, V. M. The correlation between dispersion measure and X-ray column density from radio pulsars. *Astrophys. J.* **768**, 64 (2013).
60. NASA High Energy Astrophysics Science Archive Research Center (Heasarc). HEASoft: unified release of FTOOLS and XANADU. *Astrophysics Source Code Library* ascl:1408.004 (2014).
61. Taghizadeh-Popp, M. et al. SciServer: a science platform for astronomy and beyond. *Astron. Comput.* **33**, 100412 (2020).
62. Lower, M. E. et al. Linear to circular conversion in the polarized radio emission of a magnetar. *Nat. Astron.* **8**, 606–616 (2024).
63. Oswald, L. S., Karastergiou, A. & Johnston, S. Pulsar polarization: a partial-coherence model. *Mon. Not. R. Astron. Soc.* **525**, 840–853 (2023).
64. Tremblay, P. E., Ludwig, H. G., Steffen, M., Bergeron, P. & Freytag, B. Solution to the problem of the surface gravity distribution of cool DA white dwarfs from improved 3D model atmospheres. *Astron. Astrophys.* **531**, L19 (2011).
65. Blouin, S., Dufour, P., Allard, N. F. & Kilic, M. A new generation of cool white dwarf atmosphere models. II. A DZ star with collision-induced absorption. *Astrophys. J.* **867**, 161 (2018).
66. Bédard, A., Bergeron, P., Brassard, P. & Fontaine, G. On the spectral evolution of hot white dwarf stars. I. A detailed model atmosphere analysis of hot white dwarfs from SDSS DR12. *Astrophys. J.* **901**, 93 (2020).
67. Green, G. M., Schlafly, E., Zucker, C., Speagle, J. S. & Finkbeiner, D. A 3D dust map based on Gaia, Pan-STARRS 1, and 2MASS. *Astrophys. J.* **887**, 93 (2019).
68. Hu, C.-P., Ng, C. Y. & Ho, W. C. G. A systematic study of soft X-ray pulse profiles of magnetars in quiescence. *Mon. Not. R. Astron. Soc.* **485**, 4274–4286 (2019).
69. Turolla, R. & Esposito, P. Low-magnetic magnetars. *Int. J. Mod. Phys. D* **22**, 1330024–163 (2013).
70. Tiengo, A. et al. A variable absorption feature in the X-ray spectrum of a magnetar. *Nature* **500**, 312–314 (2013).
71. Rodríguez Castillo, G. A. et al. The outburst decay of the low magnetic field magnetar SWIFT J1822.3–1606: phase-resolved analysis and evidence for a variable cyclotron feature. *Mon. Not. R. Astron. Soc.* **456**, 4145–4155 (2016).
72. Caleb, M. & Lenc, E. An emission state switching radio transient with a 54 minute period. *Zenodo* <https://doi.org/10.5281/zenodo.10989868> (2024).

Acknowledgements

M.C. thanks E. Sadler, R. Ekers, D. Huber, L. Oswald and S. Osłowski for valuable discussions. This paper makes use of data from MeerKAT (project ID DDT-20210125-MC-01) and Parkes (project ID PX079). M.C. thanks SARAO for the approval of the MeerKAT DDT request, the science operations, CAM/CBF and operator teams for their time and effort invested in the observations, and the ATNF for scheduling

observations with the Parkes radio telescope. The MeerKAT telescope is operated by the South African Radio Astronomy Observatory, which is a facility of the National Research Foundation, an agency of the Department of Science and Innovation (DSI). TRAPUM observations used the FBFUSE and APSUSE computing clusters for data acquisition, storage and analysis. These clusters were funded and installed by the Max-Planck-Institut für Radioastronomie and the Max-Planck-Gesellschaft. This scientific work uses data obtained from telescopes within the Australia Telescope National Facility (<https://ror.org/05qajvd42>), which is funded by the Australian Government for operation as a National Facility managed by CSIRO. The Parkes radio telescope (Murriyang) is part of the Australia Telescope National Facility (<https://ror.org/05qajvd42>), which is funded by the Australian Government for operation as a National Facility managed by CSIRO. We acknowledge the Wiradjuri people as the Traditional Owners of the observatory site. Inyarrimanha Ilgari Bundara/the Murchison Radio-astronomy Observatory is the site of the CSIRO ASKAP radio telescope. We acknowledge the Wajarri Yamaji as the Traditional Owners and native title holders of the observatory site. Operation of ASKAP is funded by the Australian Government with support from the National Collaborative Research Infrastructure Strategy. ASKAP uses the resources of the Pawsey Supercomputing Research Centre. Establishment of Inyarrimanha Ilgari Bundara, the CSIRO Murchison Radio-astronomy Observatory, ASKAP and the Pawsey Supercomputing Research Centre are initiatives of the Australian Government, with support from the Government of Western Australia and the Science and Industry Endowment Fund. This paper includes archived data obtained through the CSIRO ASKAP Science Data Archive, CASDA (<http://data.csiro.au>). The National Radio Astronomy Observatory is a facility of the National Science Foundation operated under cooperative agreement by Associated Universities, Inc. Construction and installation of VLITE was supported by the NRL Sustainment Restoration and Maintenance fund. M.C. acknowledges support of an Australian Research Council Discovery Early Career Research Award (project number DE220100819) funded by the Australian Government. Parts of this research were conducted by the Australian Research Council Centre of Excellence for Gravitational Wave Discovery (OzGrav), project number CE170100004. R.M.S. and N.H.-W. acknowledge support through Australian Research Council Future Fellowships FT190100155 and FT190100231, respectively. T.E.C. and S.G. acknowledge that basic research in Radio Astronomy at the US Naval Research Laboratory is supported by 6.1 Base Funding. K.M.R acknowledges support from the Vici research programme 'ARGO' with project number 639.043.815, financed by the Dutch Research Council (NWO).

Author contributions

M.C. drafted the paper with suggestions from all co-authors and is the principal investigator of the MeerKAT data. M.C. reduced and analysed the MeerKAT TUSE/PTUSE data and undertook the timing analyses along with R.M.S. E.L. calibrated, imaged and performed astrometry

on the ASKAP and MeerKAT data. D.L.K., T.M., L.F., K.M.R., N.H.-W., S.M., C.M.L.F., J.W.T.H., M.K., J.P. and B.W.S. contributed to discussions about the nature of the source. Y.P.M. analysed the MeerKAT APSUSE data and performed the beam subtraction. S.G. and T.E.C. performed the VLITE archive search, imaging and analyses. S.D.H. performed the VLA and GMRT archive search, imaging and analyses. M.E.L. performed the Faraday conversion analysis and is the principal investigator of the Parkes PX079 project. V.R. performed the Keck observations and calibration of the optical data. E.D.B. built and designed the beamformer used by MeerTRAP. S.B. scheduled the MeerKAT observations. C.M.L.F. interpreted the optical spectrum along with M.C. B.W.S. is the principal investigator of MeerTRAP.

Funding

Open access funding provided by the University of Sydney

Competing interests

The authors declare no competing interests.

Additional information

Extended data is available for this paper at <https://doi.org/10.1038/s41550-024-02277-w>.

Correspondence and requests for materials should be addressed to M. Caleb or E. Lenc.

Peer review information *Nature Astronomy* thanks Chia Min Tan and the other, anonymous, reviewer(s) for their contribution to the peer review of this work.

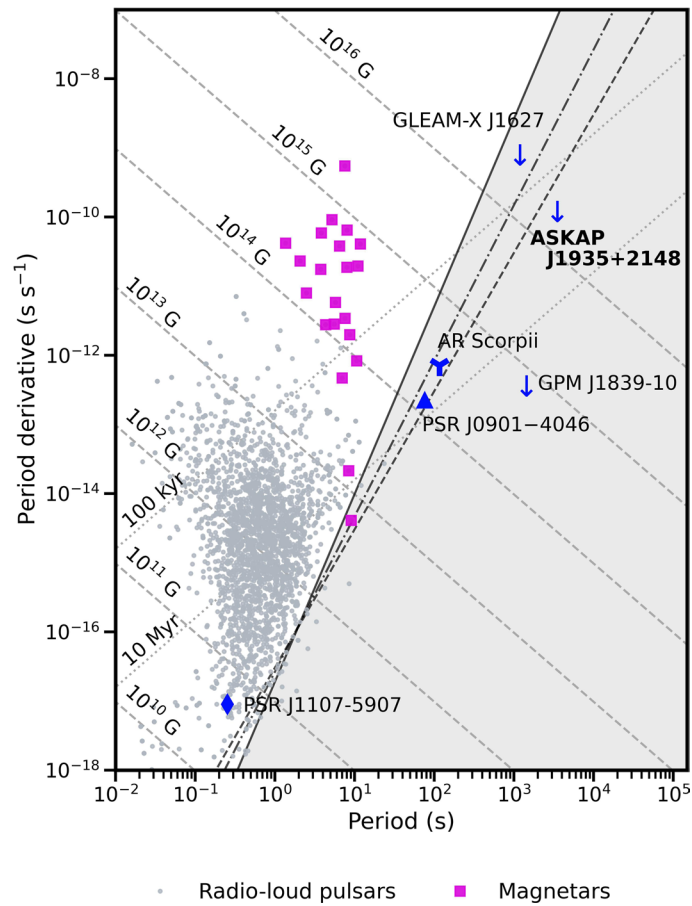
Reprints and permissions information is available at www.nature.com/reprints.

Publisher's note Springer Nature remains neutral with regard to jurisdictional claims in published maps and institutional affiliations.

Open Access This article is licensed under a Creative Commons Attribution 4.0 International License, which permits use, sharing, adaptation, distribution and reproduction in any medium or format, as long as you give appropriate credit to the original author(s) and the source, provide a link to the Creative Commons licence, and indicate if changes were made. The images or other third party material in this article are included in the article's Creative Commons licence, unless indicated otherwise in a credit line to the material. If material is not included in the article's Creative Commons licence and your intended use is not permitted by statutory regulation or exceeds the permitted use, you will need to obtain permission directly from the copyright holder. To view a copy of this licence, visit <http://creativecommons.org/licenses/by/4.0/>.

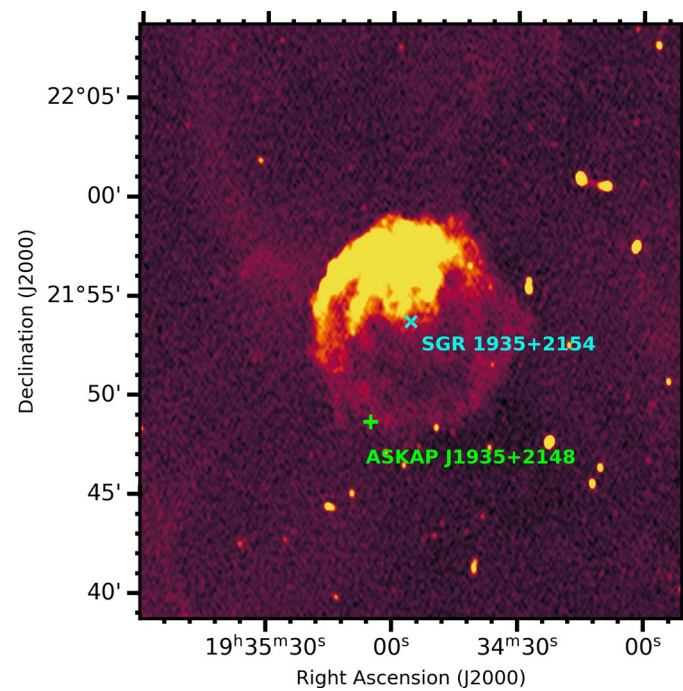
© The Author(s) 2024

¹Sydney Institute for Astronomy, School of Physics, The University of Sydney, Sydney, New South Wales, Australia. ²ARC Centre of Excellence for Gravitational Wave Discovery (OzGrav), Hawthorn, Victoria, Australia. ³Australia Telescope National Facility, CSIRO, Space and Astronomy, Epping, New South Wales, Australia. ⁴Center for Gravitation, Cosmology, and Astrophysics, Department of Physics, University of Wisconsin-Milwaukee, Milwaukee, WI, USA. ⁵Max-Planck-Institut für Radioastronomie, Bonn, Germany. ⁶Centre for Astrophysics and Supercomputing, Swinburne University of Technology, Hawthorn, Victoria, Australia. ⁷Mathematical Sciences Institute, The Australian National University, Canberra, Australian Capital Territory, Australia. ⁸ASTRON, The Netherlands Institute for Radio Astronomy, PD Dwingeloo, The Netherlands. ⁹Astrophysics, University of Oxford, Oxford, UK. ¹⁰Remote Sensing Division, US Naval Research Laboratory, Washington DC, USA. ¹¹International Centre for Radio Astronomy Research, Curtin University, Bentley, Western Australia, Australia. ¹²Department of Engineering and Physics, Sweet Briar College, Sweet Briar, VA, USA. ¹³Cahill Center for Astronomy and Astrophysics, California Institute of Technology, Pasadena, CA, USA. ¹⁴Owens Valley Radio Observatory, California Institute of Technology, Big Pine, CA, USA. ¹⁵South African Radio Astronomy Observatory (SARAO), Cape Town, South Africa. ¹⁶Jodrell Bank Centre for Astrophysics, Department of Physics and Astronomy, The University of Manchester, Manchester, UK. ¹⁷These authors contributed equally: M. Caleb, E. Lenc. ✉ e-mail: manisha.caleb@sydney.edu.au; emil.lenc@csiro.au

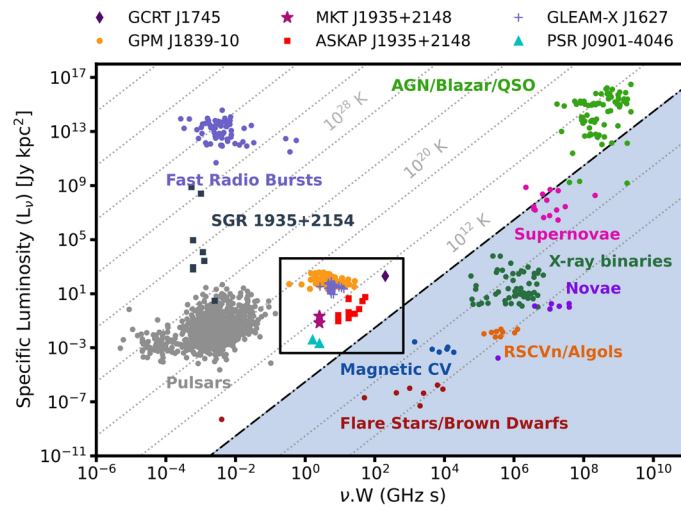


Extended Data Fig. 1 | $P - \dot{P}$ diagram showing the spin-period against the period derivative for neutron stars as reported in the ATNF pulsar catalog, and published long period transients. Lines of constant age and magnetic field for neutron stars are shown as dotted and dashed lines respectively. The lower right region of the figure bounded by the various death lines represents the

'death valley' where sources below these lines are not expected to emit in the radio. The solid death line represents Equation 9 in³⁷. In dot-dashed and dashed are the death lines modeled on curvature radiation from the vacuum gap and SCLF models as shown by Equations 4 and 9 respectively in³⁸.

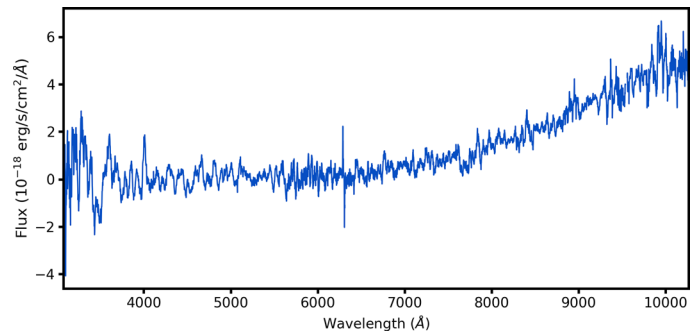


Extended Data Fig. 2 | ASKAP deep image centered on SGR 1935+2154. The data span 6 hours with a median rms of $42 \mu\text{Jy}/\text{beam}$. The position of ASKAP J1935 + 2148 places it $5''.6$ from SGR 1935 + 2154, and the $\text{DM} = 145.8 \pm 3.5$ indicates that it is in the foreground.

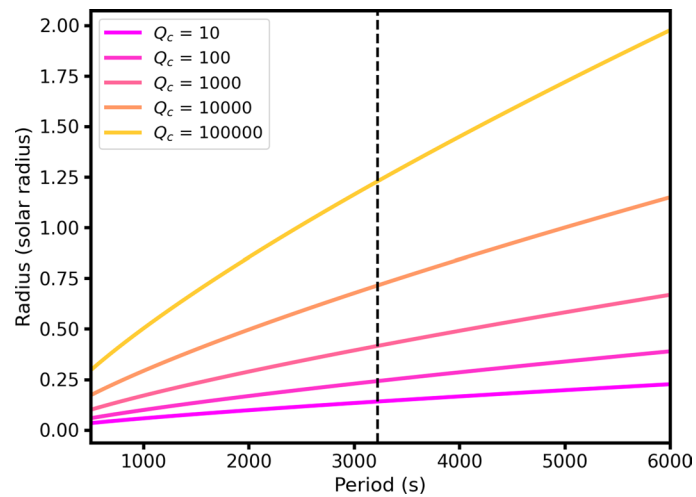


Extended Data Fig. 3 | The luminosity of different types of transients as a function of their width (W) and frequency (ν). Diagonal lines represent constant brightness temperatures. The brightness temperature of 10^{12} K separates coherent emitters from the incoherent ones, with the shaded region

(lower right triangle) housing the incoherent emitters. The long period sources shown in the legend appear to cluster together as indicated by the box, which is merely to highlight the sources and does not have a physical significance.



Extended Data Fig. 4 | Spectrum of PSO J293.7711+21.8119 using LRIS at the Keck telescope. The data shows a featureless red continuum spectrum expected of L/T-dwarf stars.



Extended Data Fig. 5 | Constraints on the radius of a source, in units of solar radii, for various assumed rotational periods. Q_c is the ratio of the field curvature radius to the stellar radius with the value inversely proportional to the size of the star. Q_c is typically assumed to be 10 for WDs but is larger in reality.

The vertical line denotes the period of ASKAP J1935 + 2148. Even in the most conservative case of $Q_c = 10$, we are able to rule out a white dwarf origin scenario. More details in Methods.

Extended Data Table 1 | ASKAP and MeerKAT observations of ASKAP J1935+2148

Epoch	SBID	Start Time UT, J2000	Duration UT, J2000	Frequency MHZ	Observation	Peak flux density mJy	Note
0	20200507-0039	2020-05-08 05:16:47	01:16:49	1284	MeerKAT	–	no detection.
0	20200510-0034	2020-05-11 03:01:01	03:17:30	1284	MeerKAT	–	no detection.
0	20200514-0008	2020-05-15 00:40:59	03:19:20	1284	MeerKAT	–	no detection.
1	44780	2022-10-12 07:00:00	06:02:35	887.5	AS113.66	6.9	one 7σ .
2	44857	2022-10-15 07:15:02	06:02:36	887.5	AS113.67	118.8, 93.7, 18.4, 17.9, 13.8	Discovery - four $> 6\sigma$; one $> 4\sigma$.
3	44918	2022-10-17 06:31:08	03:01:27	887.5	AS113.68	10.8	one $> 10\sigma$.
4	45060	2022-10-22 06:31:34	06:02:05	887.5	AS113.69	17.7, 10.2	one $> 10\sigma$ sigma; one $> 4\sigma$.
5	45086	2022-10-23 06:13:17	06:02:19	887.5	AS113.70	234.7, 209.3, 170.7, 146.6, 112.5	five $> 6\sigma$.
6	45416	2022-11-05 05:01:15	06:02:00	887.5	AS113.71	4.0	one $> 4\sigma$.
7	46350	2022-12-13 02:27:01	05:23:05	887.5	CRACOTest_A	–	no detection.
8	46419	2022-12-14 02:16:02	06:02:08	887.5	CRACOTest_A	–	no detection.
9	46492	2022-12-15 04:15:00	05:01:49	887.5	CRACOTest_B	–	no detection.
10	46554	2022-12-16 02:07:02	05:02:10	887.5	CRACOTest_B	–	no detection.
11	20230203-0012	2023-02-03 09:55:15	01:00:12	1284	MeerKAT	9.0, 2.3	DDT - one pulse and weak sub-pulse.
12	47635	2023-02-04 04:20:38	01:02:24	887.5	ULP2	–	no detection.
13	48611	2023-02-25 21:33:58	06:03:32	887.5	CRACO_ULP2	–	no detection.
14	20230302-0029	2023-03-04 06:48:46	00:59:56	1284	MeerKAT	–	DDT - no detection.
15	20230409-0012	2023-04-10 03:06:57	00:59:49	1284	MeerKAT	–	DDT - no detection.
16	20230508-0002	2023-05-08 01:41:45	01:00:10	1284	MeerKAT	2.9, 1.1	DDT - one pulse and weak sub-pulse.
17	20230821-0011	2023-08-21 16:46:25	01:00:12	1284	MeerKAT	–	DDT - no detection.

The first three rows labelled Epoch 0 are archival observations targeting SGR 1935+2154, while the rest are follow-up observations targeting ASKAP J1935+2148. See the text for details.

Extended Data Table 2 | Archival Chandra observations

ObsID	Date	DOI
21305	2019-11-24	doi: https://doi.org/10.25574/213051
21306	2019-12-03	doi: https://doi.org/10.25574/21306
22431	2020-04-30	doi: https://doi.org/10.25574/22431
22432	2020-05-02	doi: https://doi.org/10.25574/22432
23251	2020-05-18	doi: https://doi.org/10.25574/23251

The five *Chandra* observations total 157.7 ks of exposure. For all observations ASKAP J1935+2148 was located on a front-illuminated CCD: ACIS-S2 for 21305/21306 and ACIS-S4 for the remainder. See the text for details.